Applied Materials Today 13 (2018) 359–369

Contents lists available at ScienceDirect

Applied Materials Today

journal homepage: www.elsevier.com/locate/apmt

Photonic materials for high-temperature applications: Synthesis and characterization by X-ray ptychographic tomography

Kaline P. Furlan[a,b,*], Emanuel Larsson[c], Ana Diaz[d], Mirko Holler[d], Tobias Krekeler[e], Martin Ritter[e], Alexander Yu. Petrov[f,g], Manfred Eich[f], Robert Blick[b], Gerold A. Schneider[a], Imke Greving[c], Robert Zierold[b,*], Rolf Janßen[a,*]

[a] Institute of Advanced Ceramics, Hamburg University of Technology, Denickestraße 15, 21073 Hamburg, Germany
[b] Center for Hybrid Nanostructures, Universität Hamburg, Luruper Chaussee 149, 22607 Hamburg, Germany
[c] Institute of Materials Research, Helmholtz-Zentrum Geesthacht, Max-Planck-Strasse 1, 21502 Geesthacht, Germany
[d] Paul Scherrer Institut, 5232 Villigen PSI, Switzerland
[e] Electron Microscopy Unit, Hamburg University of Technology, Eißendorfer Straße 42, 21073 Hamburg, Germany
[f] Institute of Optical and Electronic Materials, Hamburg University of Technology, Eißendorfer Straße 38, 21073 Hamburg, Germany
[g] ITMO University, 49 Kronverkskii Avenue, 197101 St. Petersburg, Russia

ARTICLE INFO

Article history:
Received 12 July 2018
Received in revised form
19 September 2018
Accepted 7 October 2018

Keywords:
Ptychography X-ray computed tomography
3D image analysis
Low-temperature atomic layer deposition
Photonic materials
High-temperature applications

ABSTRACT

Photonic materials for high-temperature applications need to withstand temperatures usually higher than 1000 °C, whilst keeping their function. When exposed to high temperatures, such nanostructured materials are prone to detrimental morphological changes, however the structure evolution pathway of photonic materials and its correlation with the loss of material's function is not yet fully understood. Here we use high-resolution ptychographic X-ray computed tomography (PXCT) and scanning electron microscopy (SEM) to investigate the structural changes in mullite inverse opal photonic crystals produced by a very-low-temperature (95 °C) atomic layer deposition (ALD) super-cycle process. The 3D structural changes caused by the high-temperature exposure were quantified and associated with the distinct structural features of the ceramic photonic crystals. Other than observed in photonic crystals produced via powder colloidal suspensions or sol-gel infiltration, at high temperatures of 1400 °C we detected a mass transport direction from the nano pores to the shells. We relate these different structure evolution pathways to the presence of hollow vertexes in our ALD-based inverse opal photonic crystals. Although the periodically ordered structure is distorted after sintering, the mullite inverse opal photonic crystal presents a photonic stopgap even after heat treatment at 1400 °C for 100 h.

1. Introduction

Photonic crystals are three-dimensional periodically ordered structures with the capability of affecting the propagation of electromagnetic radiation by a photonic band-gap [1]. The spectral range in which the reflection of radiation occurs is defined by the spatial ordering of the structure and its refractive index. This selective radiation propagation behavior is attractive for a variety of technological applications, such as thermo photovoltaic energy conversion devices and also next-generation thermal barrier coatings (photonic TBCs) [2–4]. However, when exposed to high temperatures (usually higher than 1000 °C), photonic crystal structures may undergo several morphological changes, such as dimensional distortion due to sintering shrinkage or phase transformation, extensive grain growth, and in extreme cases loss of the periodical order [5], thereby impairing its photonic properties. Needless to say, the retention of these high-surface area 3D structure for high-temperature applications remains a significant challenge [5].

Since the structural characteristics and 3D phase morphology of these photonic materials dictate how they interact with electromagnetic radiation, information and knowledge about the relationship between the material's 3D structure and its photonic properties, before and after exposure to such high temperatures, is crucial for a complete understanding of the material's behavior and its application. As the arrangement of the photonic material's nanostructure might determine its effective properties and

* Corresponding authors.
E-mail addresses: kaline.furlan@tuhh.de (K.P. Furlan), rzierold@physnet.uni-hamburg.de (R. Zierold), janssen@tuhh.de (R. Janßen).

https://doi.org/10.1016/j.apmt.2018.10.002

performance, there is a driving force for more precise, high-resolution characterization methods.

When analyzing the morphology of inverse opal photonic crystals, scanning electron microscopy (SEM) is still the main technique used. Although being a fast and simple tool, several limitations arise when dealing with oxide-based inverse opal photonic crystals. First of all, they are usually non-conductive, thereby prone to charging and mechanical drift, which causes image artifacts and scanning flaws. Furthermore, if the samples are to be further exposed to high temperatures, they cannot be coated with conductive material, which could burn-out, melt or react with the structure. Moreover, the roughness associated to such a conductive coating, or even the thickness (usually 5–15 nm), could conceal some of the nano metric structural features of photonic crystals. On top of that, only qualitative 2D information of either the top view or cross sections with a limited area of investigation are obtained. Meanwhile, transmission electron microscopy (TEM) imaging is only capable of analyzing very tiny areas of the whole inverse opal photonic crystal structure, after very careful and time-consuming sample preparation. Besides that, TEM involves a strong interaction between the electrons of the primary beam and the material itself, which in turn can influence the structure and lead to artifacts, and requires a high-vacuum environment. FIB-tomography on the other hand could be used to obtain high-resolution 3D structural information, however this is a destructive technique. Furthermore, for highly porous materials an infiltration step with epoxy or conductive material is required, in order to avoid excessive sample drift, which would cause variations in the prescribed slice thickness and even loss of information in the *z*-axis direction (anisotropic resolution) [6].

Alternatively, X-ray computed tomography is a powerful non-destructive technique to investigate the inner structure morphology of porous materials [7–9], such as the inverse opal photonic crystals, in a multi length scale approach. In case of the samples studied herein, the resolution of microtomography (micrometer scale) is not enough, but synchrotron tomography, more specifically, ptychographic X-ray computed tomography (PXCT), can image different structural features from the micrometer to the nanometer scale with high resolution, even in air at atmospheric pressure [10,11].

The fabrication process defines the final structure and composition of a photonic material, and therefore, its photonic properties. Inverse opal photonic crystals are usually produced by the infiltration of a polymeric template, also referred to as a direct photonic crystal, which can be assembled by a variety of routes [12]. Infiltration techniques include sol-gel [13], colloidal routes [14,15], chemical vapor deposition (CVD) [16] and atomic layer deposition (ALD) [17]. Inverse opal photonic crystals can also be fabricated in a single-step approach, described as co-deposition [18,19]. Depending on the chosen fabrication technique, a variety of ceramic inverse opal photonic crystal materials can be produced, such as silica [19], titania [17], alumina [14], zirconia [15] and yttria stabilized zirconia (YSZ) [18]. When ranking the techniques, ALD is by far the one with the highest capability for uniform coating of such high aspect ratio structures, by which very high filling fractions and infiltration homogeneity are reported [20]. Moreover, ALD bases on successive, alternating reactions between precursors and substrate, with excellent film thickness control (on the Ångstrom-scale) and compositional control [21], even for complex systems such as ternary and quaternary oxides [22]. By ALD, tailor-made atomically mixed systems can be realized, such as mullite, a known refractory ceramic system with high-temperature stability.

Deposition of mullite films on planar substrates, not photonic structures, has already been demonstrated by CVD [23], electron beam physical vapor deposition (EB-PVD) [24] and plasma spraying [25]. However, all these processes run at considerably high or very high temperatures, i.e. 600 °C [24], 1200 °C [23] or even higher (>1800 °C) [25], which makes them unviable for infiltration of polymeric templates. In our previous work [26], we demonstrated the possibility of infiltrating Al_2O_3 inverse opal photonic crystals with mullite by ALD super-cycles performed at 150 °C. This deposition temperature is already considered low for ALD [21], however still too high for possible infiltration of polymeric templates, usually based on polystyrene or polymethylmethacrylate latex particles with glass transition temperatures of around 100 °C [27]. At temperatures usually used in ALD, polymeric templates may not only decompose, but also be oxidized during oxidant exposure [28], especially in case of ozone [29]. Furthermore, already established ALD cycle parameters for inorganic materials, may not be adequate for polymeric templates, due to the different surfaces characteristics, resulting in possible different growth mechanisms [30].

In this work, we studied the feasibility of two very-low-temperature (95 °C) atomic layer deposition processes to produce mullite inverse opal photonic crystals by infiltration of polystyrene direct photonic crystals prepared by vertical convective self-assembly. The inverse opal photonic crystal 3D structures were characterized before and after heat treatment by X-ray diffraction (XRD), SEM and PXCT [10,11] at a 3D isotropic resolution of 52 nm. The high-resolution imaging by PXCT enabled the quantification of 3D structural modifications caused by the high-temperature exposure. We demonstrate that this non-destructive technique enables the characterization of the structural features of inverse opal photonic crystals at varied scales, hardly identified by other techniques. Furthermore, the quantification of the structural changes of distinct features clarifies the pathway for structural destabilization with the temperature. Although some structural features of the photonic crystal presented relevant dimensional changes after heat treatment, a photonic stopgap was identified even after heat treatment at 1400 °C for 100 h, an outstanding behavior for a photonic crystal concerning the temperature stability [5] for high-temperature applications.

2. Materials and methods

A vertical convective self-assembly process was used to form direct photonic crystals of monodisperse polystyrene particles (762 ± 22 nm, Microparticles GmbH) onto sapphire substrates (⟨1−102⟩, Ø 30 mm × 0.53 mm, Crystec GmbH). Before immersion into the PS-water suspensions (1.0 mg ml^{-1}), the substrates were cleaned by 1-h sonication in a 1 wt.% detergent (Mucasol Brand, Merz Hygiene GmbH) deionized water (diH_2O) solution, followed by brushing, diH_2O rinsing and drying with nitrogen gas. Moreover, they were further cleaned and their surfaces were activated by an oxygen plasma treatment for 20 min (Polaron PT7160, Quorum Technologies). The colloidal crystal growth was performed inside a humidity chamber (Memmert HCP 108), at 70% RH and 55 °C for 168 h.

Atomic layer deposition was performed at a very-low-temperature of 95 °C in a super-cycle approach under a full exposure mode in a Savannah™ 100 reactor (Veeco-Cambridge Nanotech) and in a home-made reactor (University of Hamburg, Physics Department, CHyN – Center for Hybrid Nanostructures), using nitrogen as carrier gas. The ratio of Al_2O_3:SiO_2 in the inverse opal photonic crystals structure was varied by the number of internal loops within the super cycle (refer to Table S1). The precursors used for the depositions were diH_2O, trimethylaluminum, min. 98% (TMA, Strem Chemicals), (3-aminopropyl)triethoxysilane, 98% (APTES, Sigma Aldrich), ozone (OzoneLab™, OL80 W) and tris(dimethylamino)silane, 99+% (TDMAS, Strem chemicals).

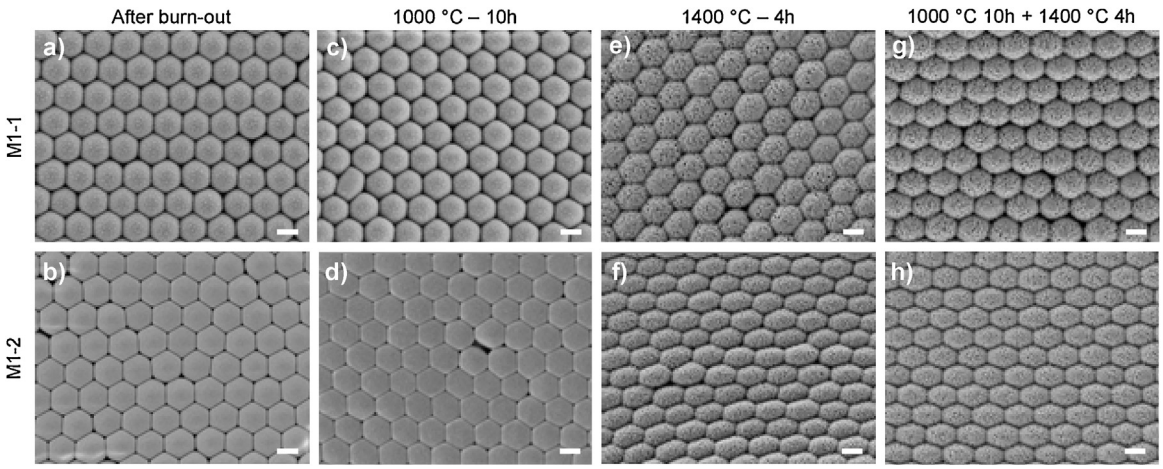

Fig. 1. Comparison between the top view morphology of inverse opal photonic crystals imaged by SEM (a, b) after burn-out and after a variety of heat treatments performed at (c, d) 1000 °C for 10 h, (e, f) 1400 °C for 4 h and (g, h) 1000 °C for 10 h plus 1400 °C for 4 h. On top are samples produced in the ALD super cycle M1-1 and on the bottom super cycle M1-2. Scale bars correspond to 500 nm.

Further details are available at the Table S1 and the Data in Brief related article.

After infiltration of the direct photonic crystals (PS templates) by ALD, the samples were heated up in a Muffle furnace in air for polymer burn-out (0.8 °C min^{-1}, 500 °C, 30 min), generating the inverse opal photonic crystals, which were later characterized. Their thermal stability was assessed by heat treatments performed under air atmosphere at different temperatures and dwell times up to 1500 °C (refer to Table S2). The inverse opal photonic crystals top view and cross section 2D structural morphology was analyzed by scanning electron microscopy (SEM, Zeiss Supra 55 VP). Phase identification was performed by Grazing incidence X-ray diffraction analysis [31] (Bruker AXS D8 Advance, Cu Kα, 40 kV, 40 mA, step size 0.01°, step time 5 s, incident beam glancing angle 1.5°). Further details of the crystal structure investigations may be obtained from the Fachinformationszentrum Karlsruhe, 76344 Eggenstein-Leopoldshafen (Germany), on quoting the depository numbers CSD-156191 and CSD-66448 (mullite), CSD-173625 (alumino-silicate), CSD-36233 (gippsite), CSD-39104 (eta Al_2O_3) and CSD-60419 (alpha alumina) or at the Crystallography Open Database (COD) on quoting the pattern numbers indicated in figures captions and text. Optical reflection spectra were measured with a UV–vis–NIR spectrometer (Perkin-Elmer, Lambda 1050) and collected in the 0.9–1.8 μm wavelength range, before and after heat treatments.

Cylindrically shaped samples were prepared for the PXCT measurements using a FEI Helios Nanolab G3 UC FIB (for further details check the Data in Brief related article). The PXCT measurements were performed at the cSAXS beamline of the Swiss Light Source at the Paul Scherrer Institut, Switzerland. The temperature of the sample stage was 90 K and the measurements were performed at 6.2 keV photon energy. 800 projections were recorded, equally spaced in angles ranging from 0° to 180°. After alignment of the projections, the tomographic reconstruction was performed. The isotropic 3D resolution was evaluated using Fourier shell correlation (as in [32]) and resulted in 54 nm and 52 nm for the samples before and after heat treatment, respectively. Image post processing and analysis were applied on the reconstructed data set. For the quantitative 3D image analysis, 10 volume-of-interests (VOIs) with cubic shape were chosen throughout each sample (edge length of 2.65 μm, total volume of 18.60 μm^3), after a representative volume of interest (RVI-test) had been performed. A detailed description is found at the associated Data in Brief article.

3. Results and discussion

3.1. Inverse opal photonic crystal thermal stability

Both types of inverse opal photonic crystals, produced by the ALD super-cycles M1-1 and M1-2 respectively, presented the typical appearance of an ordered structure, achieved after burn-out of the PS template (⟨111⟩ plane seen in the top view from Fig. 1a and b). The highly-ordered structure is not affected by the mullite formation heat treatment, carried out in air at 1000 °C for 10 h (Fig. 1c and d). Although similar to a direct photonic crystal top view (which is a highly-ordered 3D structure of interconnected particles), it is necessary to mention that an inverse opal photonic crystal consists of a structure of 3D highly-ordered macro-pores which are interconnected through contact points at the shell, highlighted in Fig. 2. In such a structure, the macro-pore size is defined by the size of the former sacrificial polystyrene particle (sub-micron scale) and the shell size is defined by the ALD super cycle (nanometer scale). In case of inverse opal photonic crystals produced by ALD, the interstitial sites (denoted as nano pores here after – see Fig. 2) will never be completely filled, due to the nature of the ALD process, i.e. there is a limit for which the precursors can reach these sites and create a film. Beyond this limit, the interstitial site will be surrounded by shells/coatings and turn into an isolated nano-pore in the middle of the structure.

After heat treatment at 1400 °C for 4 h (Fig. 1 e–h) crystallite grains were identified in the mullite inverse opal photonic crystals for both pre-treated (1000 °C 10 h) and non-pre-treated conditions. Overall, all the analyzed structures presented quite similar morphology and no differentiation could be made between the different ALD super-cycles. The appearance of a slightly distorted lattice in Fig. 1 is just related to the sample spot and domain orientation (self-assembly domains) in relation to the beam, which is usually rotated for image acquisition. Moreover, the samples' structure remained stable even after 4 h of heat treatment at 1400 °C, which is a remarkable achievement concerning temperature stability, especially in comparison to previous reports [5]. For instance, a report presented by Tang et al. describes the structures partial collapse already at 850 °C for SiO_2 and TiO_2 structures produced by centrifugation (PMMA spheres as template) and sol–gel infiltration [33]. A sol-gel route was also used by Sokolov et al. to produce α-Al_2O_3 inverse opal photonic crystals by infiltration of PMMA templates, for which a heat treatment at 1300 °C for 4 h caused a distortion of the structure (0.93 μm and 1.58 μm macro pore

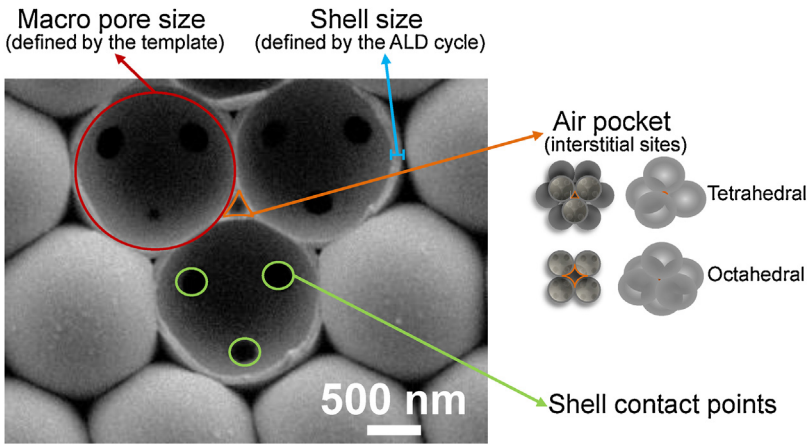

Fig. 2. Structural features in a typical inverse opal photonic crystal. SEM, top view showing FCC plane (111) and three half-cut shells. Macro-pore (PS template particle size) is around 1.5 μm.

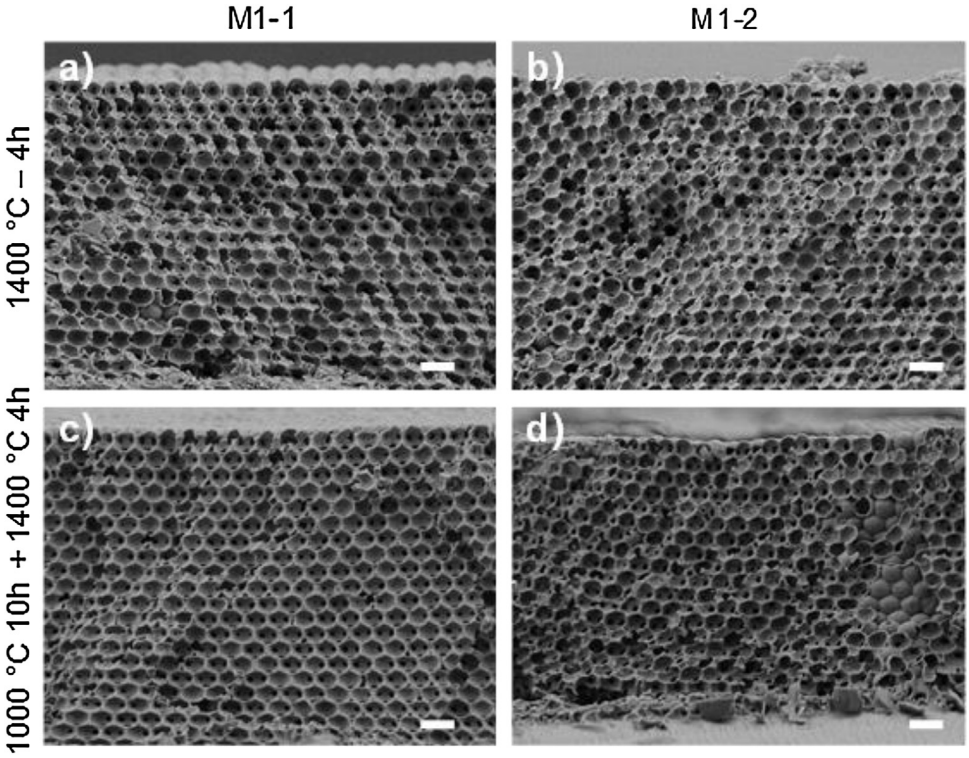

Fig. 3. Cross-sectional view of inverse opal photonic crystals imaged by SEM after heat treatment at 1400 °C for 4 h (a, b) without and (c, d) with 'mullitization' pre-treatment at 1000 °C for 10 h; (a, c) mullite inverse opal photonic crystals, cycle M1-1; (b, d) mullite inverse opal photonic crystals, cycle M1-2. The debris and different viewing planes in the picture originated during sectioning due to mechanical fracture. Scale bars represent 1 μm.

size) or even full destruction, forming a vermicular-like structure (0.4 μm macro pore size) [13]. A more stable inverse opal photonic crystal of YSZ was presented by Lashtabeg et al. [34]. Although the authors claim structural stability up to 1400 °C, accentuated sintering and grain growth can already be observed at 1100 °C, while in the structure heat treated at 1400 °C a loss in the structural ordering is clearly identified at the SEM images (reflectance measurements were not presented, as this was not the application focus). $La_{0.8}Sr_{0.2}MnO_3$/YSZ inverse opal photonic crystals produced by sol–gel infiltration of PS templates (0.35 μm macro pore size) were studied by Zhang et al. and, in contrast, a thermal stability up to only 1100 °C in conventional firing was reported [35]. Titania [17] and alumina [36] inverse opal photonic crystals also produced by ALD showed partial structural stability in air up to only 1000 °C and 1200 °C, respectively, however with significant grain growth [17] and cracks [36]. In contrast to these literature studies, the structures of the mullite inverse opal photonic crystals produced herein were stable over its total thickness as shown by the cross-section analysis (Fig. 3).

Furthermore, delamination of the inverse opal photonic crystal was only observed for the samples produced under the cycle M1-2 and at isolated spots, which overall indicates a good adhesion of the mullite inverse opal photonic crystals to the sapphire substrate. However, several cracks were observed in the overall inverse opal photonic crystal area (Ø 3 cm). Cracks are expected in such a system (mullite-sapphire) during heat cycling, due to the different thermal expansion coefficient between these materials [37], as well as the constraint imposed to the inverse opal photonic crystal

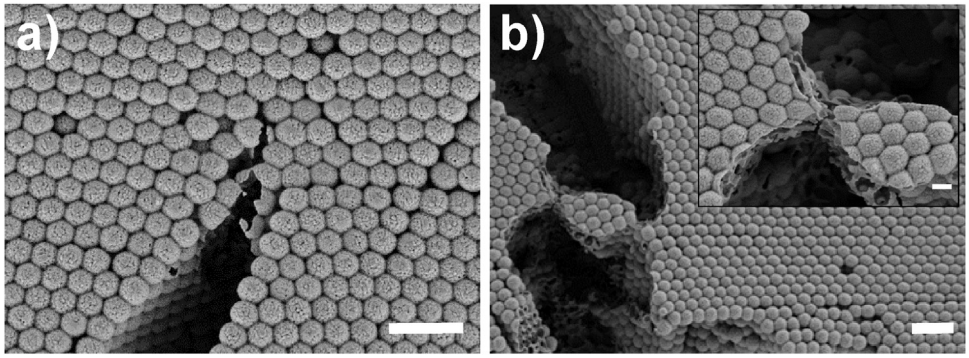

Fig. 4. Top-view SEM images of mullite inverse opal photonic crystals showing examples of cracks in between the shells. Samples heat treated at 1000 °C for 10 h plus 1400 °C for 4 h, cycle (a) M1-1 and (b) M1-2. Scale bars correspond to 2 μm and to 500 nm in the inset.

by the substrate [38], which could generate high residual stresses [39]. Cracking will occur when the stress surpasses the structure or material strength (in case of cracking in between the layers or inside the inverse opal photonic crystals structure), or the bonding strength between the inverse opal photonic crystal and substrate, for a delamination or buckling occurring without any previous crack formation, which is very unlikely to happen. It is important to point out that the ALD process is based on chemical reactions between the precursors and the exposed surfaces, which means that the inverse opal photonic crystals are chemically bonded to the sapphire substrates. Nonetheless, cracks are a usual defect in self-assembled polymer templates (colloidal spheres films), together with vacancies, Frenkel defects and screw dislocations [12]. Hence, a certain number of cracks are already existent in the polymeric template (Fig. S4) before the ALD super cycle process and are only related to the template fabrication, and not to the heat treatment or the ALD cycle. Nonetheless, image analysis of the mullite inverse opal photonic crystals (see Fig. S5), showed an average increase of 6.7% (M1-1) and 7.3% (M1-2) in the area of cracks for the samples heat treated at 1400 °C for 4 h with previous 'mullitization' treatment (1000 °C 10 h). Surprisingly, the samples heat treated at 1400 °C for 4 h showed an average value of cracks area very close to the values obtained after template burn-out (500 °C), indicating that the time at high temperatures might be a key factor for structure destabilization, even more than temperature.

The inverse opal photonic crystal itself will have residual stresses after the ALD deposition process (values for Al_2O_3 films are in the range of 250–470 MPa [40,41]), which could be maximized at the shell contact points with the substrate when compared to the contact area of a single dense film (assuming the same overall sample area). The inverse opal photonic crystal is then heated up, which could result in stress reduction (as in [41]), but also stress increase due to the thermal mismatch between the photonic crystal and the substrate. The nucleation and growth of the mullite crystallites in such structure, as well as the phase transformation of alumina phases, could also be an additional source of residual stresses. Moreover, during the heat treatment, the inverse opal photonic crystal structure starts to sinter, for which shrinkage and densification will occur (values of 9% [42] and 6% [41] are reported for Al_2O_3 films). Furthermore, as the inverse opal photonic crystal structure evolves during heat treatment and cooling (see structural features description in Fig. 2), the area section of the different features may vary over time (as shown later in the structure evolution analysis by high-resolution ptychography) and thus the absolute stress values at such points. In other words, the overall residual stress in the whole photonic crystal might be below the mechanical resistance of the 3D structure, but at such concentration points the stresses are expected to surpass even the material mechanical resistance, causing cracks and failure inside the inverse opal photonic crystal structure (see Fig. 4), which are entirely different from the self-assembly process cracks (polymeric template, see Fig. S4).

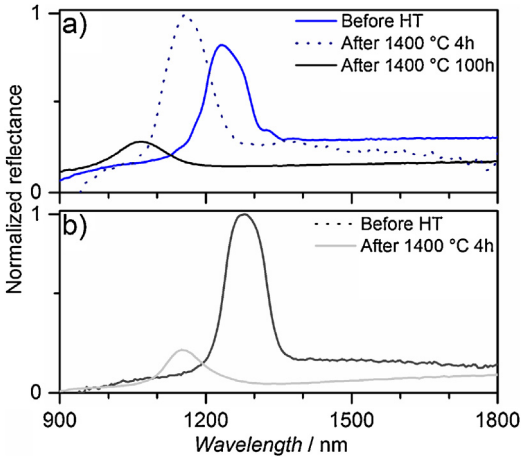

Fig. 5. Reflectance spectra of (a) mullite inverse opal photonic crystals before and after heat treatment at 1400 °C for 4 h and extensive heat treatment for 100 h; (b) Al_2O_3 inverse opal photonic crystal for comparison, showing a much higher reduction in reflectance after heat treatment at 1400 °C for 4 h than the mullite inverse opal photonic crystal.

The spectral position of the reflection peaks at normal incidence can be described by a simple equation $\lambda = 2 \times d\_111 \times n\_eff$ [2], where lambda is the wavelength, d_111 is the interplanar spacing in [111] direction of the inverse opal photonic crystal and n_eff is the average refractive index of the opal. The reflection peak position of the as-fabricated samples (before any heat treatment) corresponds to this equation. Although both photonic crystals presented a stable structure after heat treatment at 1400 °C for 4 h, only the samples produced under the cycle M1-1 still presented a photonic band-gap (Fig. 5) with a significantly higher reflectance than an alumina inverse opal photonic crystal heat treated under the same conditions. The shift of the peak to longer wavelength might be a result of increased n_eff after the mixture of SiO_2 and Al_2O_3 layers during heat treatment, or increase of the shell density, analogous to the results presented by Wang et al. for ALD Al_2O_3 films [43]. This is an interesting optical effect which needs further investigation. Further extensive heat treatment at 1400 °C for 100 h caused the reflectance peak to be reduced in intensity and shifted to the left. This observed shift can be attributed to the vertical shrinkage of the structure and thus reduction of d_111, while the reduction in intensity could be associated to the opening of microscopic cracks due to structure sintering, as well as the texture of mullite grains on the structure shells (compare Fig. 1a and b and g and h. Even though

the reflectance was reduced and shifted, the presence of a photonic stopgap after extensive heat treatment at 1400 °C for 100 h is remarkable [5], especially because the inverse opal photonic crystal structure seems to be disordered (Fig. S6). This could be related to some reminiscent periodical modulation in the vertical direction.

After extensive heat treatment at 1400 °C for 100 h, the inverse opal photonic crystals presented a clearly sintered structure, with the occurrence of abnormal grain growth (see white arrows in Fig. S6) and delamination. Besides, the sample produced under the cycle M1-1 (higher Al_2O_3 content) presented an apparent slightly more refined structure than the samples produced under the cycle M1-2. In both samples, grains with varied sizes and faceted appearance were observed. Astonishingly, the samples are still quite porous. Pores were also observed in the samples heat treated at 1500 °C for 8 h (Fig. S7). Although the sample M1-1 still presented the shape of the former structure shells, no photonic band-gap was identified (Fig. S8), associated to the severe delamination suffered by these samples. The samples from cycle M1-2 presented the formation of acicular grains, resembling the mullite microstructures encountered in common powder metallurgy products.

3.2. Mullite phase formation

After ALD and burn-out, the inverse opal photonic crystals within this study were still amorphous, although the sample from the cycle M1-1 (refer to the associated Data in Brief article for ALD cycle details) presented one peak (Fig. S1) that could be associated to Gippsite (transition Al_2O_3 phase, COD #9015976). The very low-deposition temperature used in this study (95 °C) is far below the crystallization temperatures for alumino-silicates, but the burn-out temperature (500 °C) could already promote crystallization of Al_2O_3 transition phases [44]. The heat treatment performed at 1000 °C for 10 h (Fig. 6a) promoted the conversion of the 3D amorphous structures to mullite. Schmücker et al. [24] reported direct mullite formation (also called type I) in EB-PVD planar films, when the layer thicknesses of the Al_2O_3 and SiO_2 laminates were smaller than 5 nm [24], which was also the case in this study. However, an η-Al_2O_3 phase (COD #1541582) was also identified, which was expected, as the ALD super-cycles were designed to fit the Al_2O_3-rich region inside the Al_2O_3–SiO_2 phase diagram [45]. Since the mullite inverse opal photonic crystals are desired to be thermally stable structures, the possible presence of free silica as a glassy phase is likely to be more detrimental to this purpose [46], than the presence of alumina. Nevertheless, the temperature conversion of the mullite inverse opal photonic crystal structure is below the reported temperatures for powder mixtures [47] and diphasic sol–gels [48]. The conversion temperature observed in this study (of only about 1000 °C) is comparable with temperatures associated to direct mullite conversion of monophasic gels [48], however, without the excessive shrinkage associated to sol-gel but with ALD inherent conformal coating of the inverse opal photonic crystal structures. This low conversion temperature is associated to the high mixing of Al_2O_3 and SiO_2 in an atomistic scale provided by the ALD super-cycle process.

Moreover, although both samples presented the diffraction peaks associated to mullite, the inverse opal photonic crystals produced under the super-cycle M1-1 (refer to Table S1) fitted a mullite pattern (COD #7105575) with a slightly higher Al content than the cycle M1-2 (COD #9010159). Both patterns present phases which are very similar (most of the peak positions are nearly identical) and have orthorhombic cells, being the former slightly larger in a and c directions. This result is in agreement with the estimated Al_2O_3:SiO_2 ratio based on the ALD super-cycles and expected to be larger (lower SiO_2 content) for the cycle performed with 3DMAS than the one with APTES as silica precursor, due to the fact that for the cycle M1-2, the binary loop of the ALD super-cycle

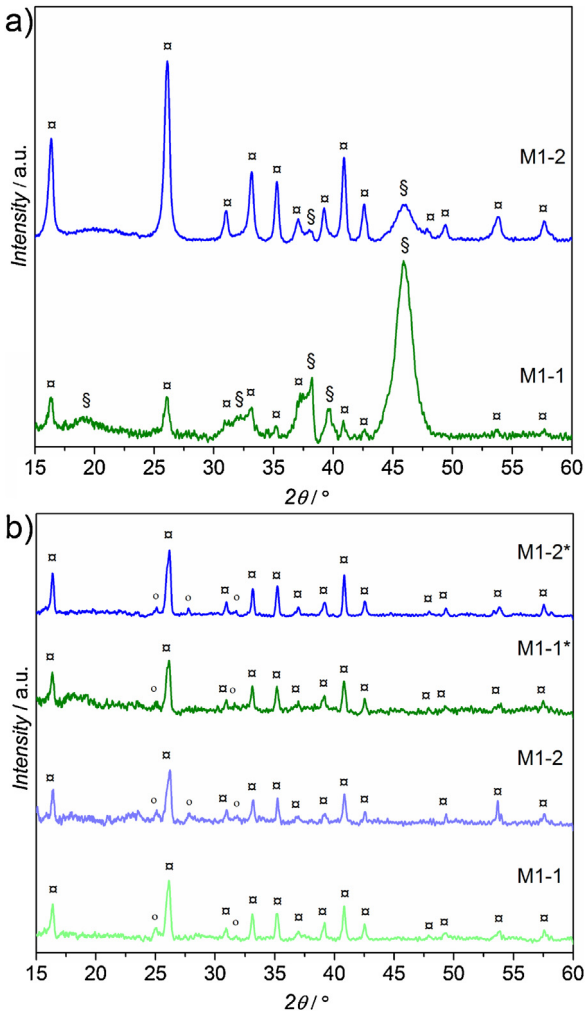

Fig. 6. XRD spectra of samples heat treated at a) 1000 °C for 10 h showing the conversion to mullite (symbol ¤ – COD #7105575 and #9010159) and small peaks related to an η-Al_2O_3 phase (symbol § – COD #1541582) and b) 1400 °C for 4 h showing the presence of mullite (symbol ¤ – COD #7105575 and #9010159) and small peaks related to an aluminum silicate phase (symbol o – COD #8103692). The symbol * indicates samples, which were previously heat treated at 1000 °C (for mullite conversion). Cycles M1-1 and M1-2 are indicated in green and blue, respectively. COD stands for Crystallography Open Database.

comprehends twice as more 'SiO_2' sub-cycles than the cycle M1-1. Therefore, more silica is introduced into the inverse opal photonic crystal structure. As the growth per cycle of the binary silica cycles are different for each precursor, a cycle performed with the APTES precursor with only one pulse of each binary cycle per super cycle (as the one performed for 3DMAS, M1-1) would fall far off the stoichiometric range for mullite, with estimated Al_2O_3 content of more than 91 wt.%. In contrast to our previous work [26], no silica-related middle band ($2\theta = 22°$) was identified, which once more corroborates the expected high-Al_2O_3 content of the mullite inverse opal photonic crystals produced in this work, which is also confirmed by energy-dispersive X-ray spectroscopy analysis (Fig. S2). These results demonstrate the high capability of tuning the material composition in ALD super cycle process, even at such a low deposition temperature of 95 °C. Furthermore, mullite manufactured by other routes often present undesired residual glassy phase from silica sources [48], even when designed to have a high Al_2O_3 content, which is not the case for the ALD super cycle processing.

The peaks associated to the mullite phase are greatly enhanced by further heat treatment of the inverse opal photonic structures at 1400 °C for 4 h. Unlike the samples heat treated at 1000 °C,

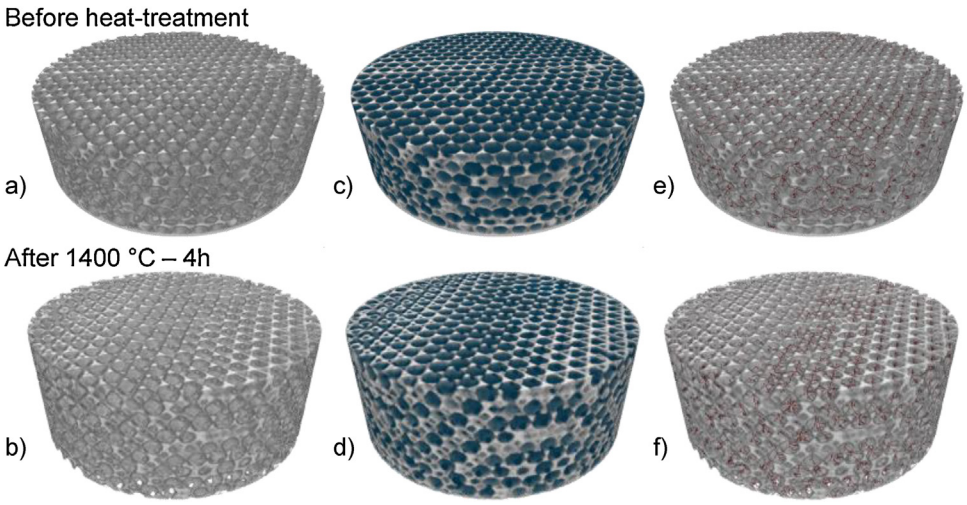

Fig. 7. 3D rendering of the PXCT tomograms from the mullite inverse opal photonic crystals (a, c, e) before and (b, d, f) after heat treatment at 1400 °C for 4 h, showing some of the structural features quantified in the image analysis: (c, d) macro pores highlighted in dark blue (e, f) image skeletons representing the interconnections between the pores. Samples' volumes are (a, c, e) 57 μm^3 and (b, d, f) 52 μm^3.

the samples did not present peaks related to an Al_2O_3 transition phase, but all the samples analyzed presented peaks identified as an alumino-silicate phase, also orthorhombic (COD #8103692). Nevertheless, the detection range for the X-ray diffraction analysis should be taken into account [49], especially considering that the measurements were performed in grazing incidence mode (1.5° as glancing angle) [31]. For this configuration, a volume associated with a smaller penetration depth is analyzed, when in comparison to the most common Bragg-brentano mode, reflecting in a global smaller volume of analysis, i.e. if a phase is present in the sample, but at a volume fraction smaller than the detection limit, than it will not be identified. Note that the mullite peaks are clearly identified even in the samples without previous heat treatment at 1000 °C (curves with symbol * in Fig. 6b), thus indicating that mullite formation occurs even for samples heat treated directly at 1400 °C (heating rate of 5 °C min^{-1}), i.e. there is no need for previous mullite formation treatment.

The peaks associated to the mullite phase are narrowed and sharpened by the extreme heat treatment at 1500 °C for 8 h (Fig. S3). This observation points to the probable growth of mullite crystallites [49], later confirmed by electron microscopy analysis. Once again, no difference was observed between the samples previously heat treated at 1000 °C for 10 h and the samples directly heat treated at 1500 °C for 8 h. Alternatively, at such extreme heat treatment, the samples produced by the ALD super cycle with estimated higher Al_2O_3 content (M1-1, 3DMAS as silica precursor) presented peaks clearly associated to the formation of alpha-alumina phase (COD #1000032), reiterating the high Al_2O_3 content in the composition of this inverse opal photonic crystal. In comparison, the samples produced by the ALD super cycle M1-2 (APTES as silica precursor), presented only peaks related to the mullite phase (COD #9010159). In our recent work with Al_2O_3 inverse opal photonic crystals [36], we have demonstrated that the α-alumina phase is formed already at 1100 °C, being the only phase present after heat treatment at 1200 °C for 1 h. However, in the hereby presented work α-alumina phase was only identified after the extreme heat treatment at 1500 °C for 8 h. This fact confirms the metastable nature [45] of the composition produced by the ALD super cycle M1-1 and also suggests a hindrance mechanism for the nucleation and growth of the α-alumina phase, which in sol-gel routes, as well as in powder metallurgy route is usually identified at much lower temperatures. Jakschik et al. have shown that the crystallization behavior of ALD Al_2O_3 films is directly affected by the film thickness, for which grains were smaller in thinner films (for the same heat treatment conditions)[50]. Their explanation was related to the higher probability of nucleation seeds in thicker films, thus reducing the thermal budget required to form crystallites. A similar trend was observed during annealing of 6 nm ALD Al_2O_3 films [41]. Even for thicker films (100 nm) deposited at 250 °C [51], crystallization is identified only after heat treatment at 825 °C. It is important to point out that these publications dealt with 'pure' Al_2O_3 films, while mullite is a ternary oxide and therefore a more complex system. Furthermore, the complex inverse opal photonic crystal morphological structure could also present, other than the low film thickness, different behavior in junction points (interstitial sites and contact points) than in the shells 'free' area (see Fig. 2). Moreover, as the heat treatment evolves the thickness of the inverse opal photonic crystals structural features may vary, as discussed later in the PXCT analysis section.

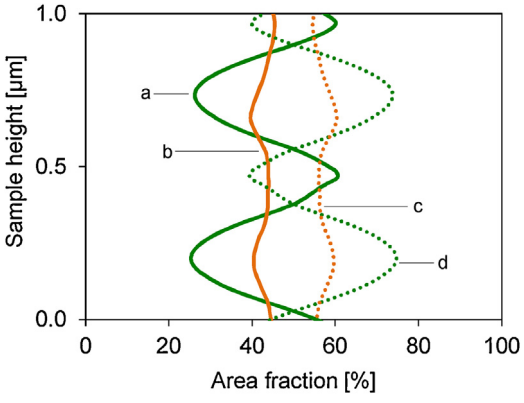

Fig. 8. Periodicity of the area fraction of inverse opal photonic crystal phase and pores, according to the sample height obtained through 2D-analysis of a set of slices. Inverse opal photonic crystal (a, d) before heat treatment and (b, c) after the heat treatment showing the (c, d) pores area fraction (macro- plus nano-pores) and (a, b) inverse opal photonic crystal area fraction. Refer to Fig. S9 for visualization of the area fraction variation in different 2D slices extracted from the PXCT dataset.

3.3. 3D structural changes analysis by high-resolution ptychography

Imaging of the samples' entire volume (Fig. 7, for details refer to the associated Data in Brief article) revealed a highly interconnected porous structure, with the highest local porosity reaching 75% for the sample before heat treatment, which is slightly above the theoretical value for FCC close packing. It is important to point out that this maximum value represents the area fraction (2D) occupied by the macro pores and their contact points, while the theoretical value only considers the spaces occupied by the macro pores, thus excluding the contact points (also referred to as necks – refer to Fig. 2 for structural features definition). As expected, the local porosity (area fraction of pores) in 2D varies depending on the sample height (Fig. 8) and it is inverse to the photonic crystal area fraction (i.e. ceramic oxide area fraction). The relationship between the maximum and minimum values of area fraction of the samples indicates a sintering of the structure, with consequent transport of matter in the inverse opal photonic crystal phase, resulting in relative different photonic crystal phase area fraction values after heat treatment. It is essential to mention, however, that this is a 2D analysis of the slices obtained from the PXCT dataset and it represents only an area fraction, therefore, comparable to the planar density of the variety of FCC planes. Whereas in the 3D analysis a volumetric average (Perc. Vol.) is obtained, which represents the inverse opal photonic crystal packing fraction.

A period of 531 nm was identified for the sample before heat treatment. This value is above the theoretical value for the distance between ⟨111⟩ planes in a FCC cell considering the original packing of the former PS spheres, indicating that the overall 3D packing of the spheres differs from the theoretical close-packed value. This observation was confirmed by the 3D quantitative analysis of packing fraction, which resulted in a volume fraction of $57.5 \pm 1.1\%$ for the macro pores phase. As mentioned above, this number is directly related to the volume fraction of the inverse opal photonic crystal phase, which was found to be $41.4 \pm 1.0\%$ for the sample before heat treatment and $42.2 \pm 1.1\%$ for the sample after heat treatment. This quite surprising result implies that the material's photonic response is influenced by the structural shrinkage (especially of macro pores) and macro cracks opening (discussed in the previous topic), rather than the overall ceramic oxide volume fraction (here named as photonic crystal phase).

An overall 8% structural shrinkage was observed for distinct features in different scales and dimensions (Fig. 9). First, this value can be extracted from the 2D periodicity shown in Fig. 8. While the period was 531 nm before heat treatment, it resulted in 488 nm after heat treatment. Next, the 3D quantitative analysis of the macro pores size also resulted in a shrinkage of 8%, from 541 ± 17 nm to 499 ± 27 nm. Finally, the contact points analysis also resulted in the same shrinkage value of 8% (135 ± 30 nm before and 124 ± 26 nm after heat treatment). Nevertheless, the volumetric shrinkage value obtained from the quantitative analysis is close to the value reported for Al_2O_3 ALD films heat treated up to 850 °C (10%), associated with film densification measured by X-ray reflectivity (XRR).

Although shrinkage was observed, the connectivity density of the 3D structure was increased from $4.94 \pm 0.94\ \mu m^{-3}$ before heat treatment to $6.48 \pm 0.49\ \mu m^{-3}$ after heat treatment, which indicates an overall opening of the inverse opal photonic crystal structure. Hereby, the connectivity density relates the pore interconnectivity of adjacent pores and is based on the nearest connecting pore available at the shortest distance, meaning that the nearest pore in the same 2D slice, for example, will not necessarily be the nearest connection point found in 3D (see Data in Brief related article).

The structure opening is supported by the analysis of the nano-pores feature (see Fig. 2). Whereas shrinkage was observed for the structural features discussed above, the nano-pores instead presented an increase in dimension (hereafter denoted as enlargement), in the range of 110 ± 46 nm before heat treatment to 122 ± 59 nm after heat treatment. The high standard deviation represents the heterogeneity of this porous structure (sphericity values were 0.80 ± 0.21 and 0.95 ± 0.32 before and after heat treatment, respectively and related to the fact that an average size is collected from both the tetrahedral and octahedral sites nano-pores population (theoretical size ratio between both features is around 0.8) [52]. This enlargement (Fig. 9c and h) is reflected by the opening of the inverse opal photonic crystal structure at such points and indicates a mass transport direction from these nano pores regions to the shells, which is entirely different from that reported for inverse opal photonic crystals produced by infiltration of polymer templates by powder colloidal suspensions [53] or sol–gel [13,33,34]. Sokolov et al. [13] presented a 2D analysis by SEM of Al_2O_3 inverse opal photonic crystals produced by sol–gel after heat treatment. Apart from the macro pore shrinkage (which was also observed in this work), a clear growth of the so-called 'vertexes' (located in the same place as the nano-pores, but filled with material) together with thinning of the struts (denoted as shells in this work) was observed.

As pointed out by our group in a former publication [36] and now strongly supported by the PXCT 3D analysis, we relate the observed differences to the different starting structures, namely the presence of additional nano-pores in our ALD-based inverse opal photonic crystals. The possible lower homogeneity (with local concentration areas) for the sol–gel and colloidal route based inverse opal photonic crystals could also contribute to the observed different behavior. All this culminates into different structure evolution pathways for differently synthesized photonic crystals.

The enlargement of nano-pores was also confirmed by the 3D analysis of the volume fraction, for which an increase of 67% in average was observed (from $1.2 \pm 0.2\%$ to $2.0 \pm 0.4\%$) and supported by earlier studies performed by Kingery and Francois [54], and Slamovich and Lange [55], for which the growth or shrinkage of a pore was related to the differential chemical potential between the curved pore surface and a flat surface or the surroundings grains, respectively. In the first study, convex pores (in this study referred to as nano-pores) were stated to always grow, while in the latter the authors claim it could either shrink or grow up to some equilibrium size. In a second study, Slamovich and Lange [56] showed that the pore behavior has a proportional correlation to the pore coordination number and intersecting grain boundaries. However, these studies were performed in powder metallurgy bulk materials, which present a wider distribution of both pores and grains sizes and shapes, while for our photonic crystals narrower distributions are expected both for pores (original PS spheres and their packing) and grains (nucleation and growth from a very homogeneous structure generated by ALD).

At last, the interpretation of the absolute values for the structural features discussed above must take into account the possible contributions from the partial volume effects and grayscale values distribution, as described in the associated Data in Brief article. Nevertheless, X-ray ptychography offers the possibility of comparing structures of relatively large samples before and after heat treatments (in situ or ex situ), which is hardly possible by other techniques such as FIB or TEM tomography. Depending on the instrument set-up it is also possible to work under varying temperatures, pressures and chemical environments. The development of the instrumentation set-up and in situ measurements of the structural changes in photonic structures induced by the temperature exposure is foreseen as future work.

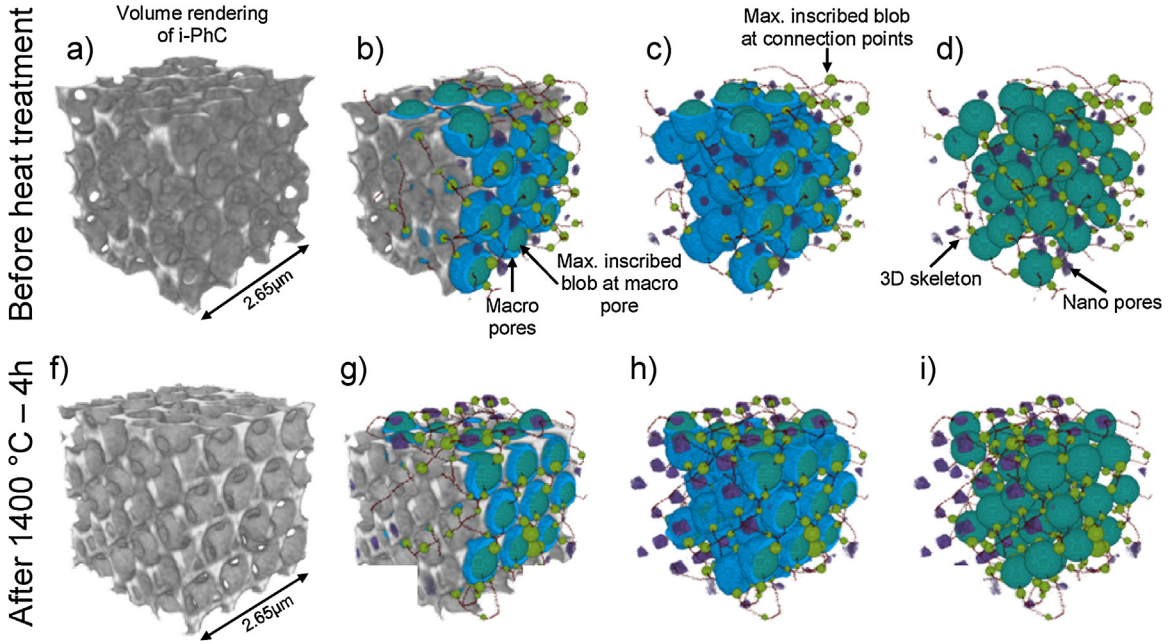

Fig. 9. 3D rendering of selected VOIs extracted from the PXCT data sets of the mullite inverse opal photonic crystals (a–d) before and (f–i) after heat treatment at 1400 °C for 4 h showing the structural features analyzed during image analysis: (a, f) inverse opal photonic crystal phase (b–d, g–i) macro pores pictured blue and inscribed blobs in green; contact points in yellow; nano pores in purple and image skeleton in red (for details see Fig. 2 and the associated Data in Brief article). A perpendicular cutting plane was applied to allow the visualization of all the structural features. Volume of the VOIs shown in (a, f) is 18.6 μm^3.

4. Conclusion

High-temperature stable inverse opal photonic crystals were produced by low-temperature (95 °C) atomic layer deposition super-cycles. Two different silica precursors were used (APTES and 3DMAS), and combined with TMA, water and ozone to generate the inverse opal photonic crystals by infiltration of the polystyrene direct photonic crystals. The both type of photonic crystals were amorphous after deposition and crystallized to mullite upon heating at 1000 °C, comparable to the mullitization temperature of sol–gels type I, attributed to the high compositional mixing homogeneity provided by ALD.

We have demonstrated the possibility of non-destructive imaging of inverse opal photonic crystals by PXCT at varied length scales, from micron-sized features to nanoscale details. The comparison between non-heat-treated and high-temperature heat-treated samples have allowed us to identify the inherent structural changes and distinct structural features at nanometer resolution. In comparison to the usual 2D analysis performed by SEM or TEM, our analysis presented in this paper can be much more useful both for the understanding of the structural destabilization with temperature, as well as an input data for simulations of the photonic response. By the complete view of the 3D structure and quantification of structural changes, associated with future simulations, we aim to optimize the structure overall and develop even more stable photonic materials.

Moreover, the mullite inverse opal photonic crystals produced in the ALD super-cycle with higher Al_2O_3:SiO_2 compositional ratio showed high-temperature stability up to 1400 °C, which might allow its application as a refractory photonic material.

Acknowledgements

We gratefully acknowledge financial support from the German Research Foundation (DFG) via SFB 986 “M3”, projects UA-UHH, C5, Z2, C2 and Z3. We also acknowledge technical staff Lisa Fitzek for some of the images acquisition at the SEM and cracks area fraction image analysis.

K.P.F was responsible for the self-assembly process, photonic crystals characterization and results analysis. K.P.F. and R.Z. were responsible for the development of the low-temperature mullite atomic layer deposition process to produce mullite inverse opal photonic crystals by polymer template infiltration. T.K. was responsible for the micro-pillars FIB preparation for the ptychography experiments conducted by H.M. and A.D at the cSAXS beamline. Analysis and quantification of the ptychography data was performed by E.L. and K.P.F. All authors contributed to results discussion, as well as manuscript preparation and have given approval to its final version.

The raw data required to reproduce these findings are available to download from https://doi.org/10.17632/zn49dsk7x6.1 (If the above link doesn’t work, please copy and paste in your browser instead of clicking).

Appendix A. Supplementary data

Supplementary data associated with this article can be found, in the online version, at doi:10.1016/j.apmt.2018.10.002.

References

[1] S. John, K. Busch, Photonic bandgap formation and tunability in certain self-organizing systems, J. Lightwave Technol. 17 (1999) 1931–1943.
[2] H.S. Lee, R. Kubrin, R. Zierold, A.Y. Petrov, K. Nielsch, G.A. Schneider, M. Eich, Thermal radiation transmission and reflection properties of ceramic 3D photonic crystals, J. Opt. Soc. Am. B 29 (2012) 450.
[3] V. Shklover, L. Braginsky, G. Witz, M. Mishrikey, C. Hafner, High-temperature photonic structures. Thermal barrier coatings, infrared sources and other applications, J. Comp. Theor. Nano 5 (2008) 862–893.
[4] Y.X. Yeng, M. Ghebrebrhan, P. Bermel, W.R. Chan, J.D. Joannopoulos, M. Soljacic, I. Celanovic, Enabling high-temperature nanophotonics for energy applications, Proc. Natl. Acad. Sci. U.S.A. 109 (2012) 2280–2285.
[5] S.G. Rudisill, Z. Wang, A. Stein, Maintaining the structure of templated porous materials for reactive and high-temperature applications, Langmuir 28 (2012) 7310–7324.
[6] K.R. Mangipudi, V. Radisch, L. Holzer, C.A. Volkert, A FIB-nanotomography method for accurate 3D reconstruction of open nanoporous structures, Ultramicroscopy 163 (2016) 38–47.
[7] M. Ogurreck, J.J. do Rosario, E.W. Leib, D. Laipple, I. Greving, F. Marschall, A. Last, G.A. Schneider, T. Vossmeyer, H. Weller, F. Beckmann, M. Muller, Determination of the packing fraction in photonic glass using synchrotron radiation nanotomography, J. Synchrotron Radiat. 23 (2016) 1440–1446.
[8] C. Ying-Chieh, J.B. Geddes, L. Yin, P. Wiltzius, P.V. Braun, X-ray computed tomography of holographically fabricated three-dimensional photonic crystals, Adv. Mater. 24 (2012) 2863–2868.
[9] S. Zabihzadeh, S. van Petegem, M. Holler, A. Diaz, L.I. Duarte, H. van Swygenhoven, Deformation behavior of nanoporous polycrystalline silver. Part I, Acta Mater. 131 (2017) 467–474.
[10] M. Dierolf, A. Menzel, P. Thibault, P. Schneider, C.M. Kewish, R. Wepf, O. Bunk, F. Pfeiffer, Ptychographic X-ray computed tomography at the nanoscale, Nature 467 (2010) 436–439.
[11] M. Holler, M. Guizar-Sicairos, E.H.R. Tsai, R. Dinapoli, E. Müller, O. Bunk, J. Raabe, G. Aeppli, High-resolution non-destructive three-dimensional imaging of integrated circuits, Nature 543 (2017) 402–406.
[12] N. Vogel, M. Retsch, C.-A. Fustin, A. Del Campo, U. Jonas, Advances in colloidal assembly: the design of structure and hierarchy in two and three dimensions, Chem. Rev. 115 (2015) 6265–6311.
[13] S. Sokolov, D. Bell, A. Stein, Preparation and characterization of macroporous α-alumina, J. Am. Ceram. Soc. 86 (2003) 1481–1486.
[14] F. Tang, H. Fudouzi, Y. Sakka, Fabrication of macroporous alumina with tailored porosity, J. Am. Ceram. Soc. 86 (2003) 2050–2054.
[15] Y. Jia, C. Duran, Y. Hotta, K. Sato, K. Watari, Macroporous ZrO_2 ceramics prepared from colloidally stable nanoparticles building blocks and organic templates, J. Colloid Interface Sci. 291 (2005) 292–295.
[16] H.M. Yates, M.E. Pemble, A. Blanco, H. Míguez, C. López, F. Meseguer, Growth of tin oxide in opal, Chem. Vap. Deposit. 6 (2000) 283–285.
[17] R.M. Pasquarelli, H.S. Lee, R. Kubrin, R. Zierold, A.Y. Petrov, K. Nielsch, G.A. Schneider, M. Eich, R. Janssen, Enhanced structural and phase stability of titania inverse opals, J. Eur. Ceram. Soc. 35 (2015) 3103–3109.
[18] R. Kubrin, J.J. do Rosario, H.S. Lee, S. Mohanty, R.P. Subrahmanyam, I. Smirnova, A. Petrov, A.Y. Petrov, M. Eich, G.A. Schneider, Vertical convective coassembly of refractory YSZ inverse opals from crystalline nanoparticles, ACS Appl. Mater. Interfaces 5 (2013) 13146–13152.
[19] J.J. do Rosário, E.T. Lilleodden, M. Waleczek, R. Kubrin, A.Y. Petrov, P.N. Dyachenko, J.E.C. Sabisch, K. Nielsch, N. Huber, M. Eich, G.A. Schneider, Self-assembled ultra high strength, ultra stiff mechanical metamaterials based on inverse opals, Adv. Eng. Mater. 17 (2015) 1420–1424.
[20] J.S. King, C.W. Neff, C.J. Summers, W. Park, S. Blomquist, E. Forsythe, D. Morton, High-filling-fraction inverted ZnS opals fabricated by atomic layer deposition, Appl. Phys. Lett. 83 (2003) 2566–2568.
[21] S.M. George, Atomic layer deposition: an overview, Chem. Rev. 110 (2010) 111–131.
[22] M.D. McDaniel, T.Q. Ngo, S. Hu, A. Posadas, A.A. Demkov, J.G. Ekerdt, Atomic layer deposition of perovskite oxides and their epitaxial integration with Si, Ge, and other semiconductors, Appl. Phys. Rev. 2 (2015) 41301.
[23] B. Armas, F. Sibieude, A. Mazel, R. Fourmeaux, M. de Icaza Herrera, Low-pressure chemical vapour deposition of mullite layers using a cold-wall reactor, Surf. Coat. Technol. 141 (2001) 88–95.
[24] M. Schmücker, W. Hoffbauer, H. Schneider, Constitution and crystallization behaviour of ultrathin physical vapor deposited (PVD) Al_2O_3/SiO_2 laminates, J. Eur. Ceram. Soc. 21 (2001) 2503–2507.
[25] K.N. Lee, R.A. Miller, N.S. Jacobson, New generation of plasma-sprayed mullite coatings on silicon carbide, J. Am. Ceram. Soc. 78 (1995) 705–710.
[26] K.P. Furlan, T. Krekeler, M. Ritter, R. Blick, G.A. Schneider, K. Nielsch, R. Zierold, R. Janssen, Low-temperature mullite formation in ternary oxide coatings deposited by ALD for high-temperature applications, Adv. Mater. Interfaces 4 (2017) 1700912.
[27] J.E. Mark, Polymer Data Handbook, 2nd ed., Oxford University Press, Oxford, New York, 2009.
[28] L. Steier, S. Bellani, H.C. Rojas, L. Pan, M. Laitinen, T. Sajavaara, F. Di Fonzo, M. Grätzel, M.R. Antognazza, M.T. Mayer, Stabilizing organic photocathodes by low-temperature atomic layer deposition of TiO_2, Sustain. Energy Fuels 1 (2017) 1915–1920.
[29] P.S. Bailey, The reactions of ozone with organic compounds, Chem. Rev. 58 (1958) 925–1010.
[30] H.C. Guo, E. Ye, Z. Li, M.-Y. Han, X.J. Loh, Recent progress of atomic layer deposition on polymeric materials, Mater. Sci. Eng. C 70 (2017) 1182–1191.
[31] T.C. Huang, P.K. Predecki, Presented at DXC on Appl. of X-ray Anal, Denver, USA, 1997.
[32] M. Holler, A. Diaz, M. Guizar-Sicairos, P. Karvinen, E. Färm, E. Härkönen, M. Ritala, A. Menzel, J. Raabe, O. Bunk, X-ray ptychographic computed

tomography at 16 nm isotropic 3D resolution, Sci. Rep. 4 (2014) 3857 EP.
[33] F. Tang, T. Uchikoshi, Y. Sakka, A practical technique for the fabrication of highly ordered macroporous structures of inorganic oxides, Mater. Res. Bull. 41 (2006) 268–273.
[34] A. Lashtabeg, J. Drennan, R. Knibbe, J.L. Bradley, G.Q. Lu, Synthesis and characterisation of macroporous yttria stabilised zirconia (YSZ) using polystyrene spheres as templates, Microporous Mesoporous Mater. 117 (2009) 395–401.
[35] N. Zhang, J. Li, W. Li, D. Ni, K. Sun, High performance three-dimensionally ordered macroporous composite cathodes for intermediate temperature solid oxide fuel cells, RSC Adv. 2 (2012) 802–804.
[36] K.P. Furlan, R.M. Pasquarelli, T. Krekeler, M. Ritter, R. Zierold, K. Nielsch, G.A. Schneider, R. Janssen, Highly porous α-Al_2O_3 ceramics obtained by sintering atomic layer deposited inverse opals, Ceram. Int. 43 (2017) 11260.
[37] Y. Hirata, S. Itoh, T. Shimonosono, S. Sameshima, Theoretical and experimental analyses of Young's modulus and thermal expansion coefficient of the alumina-mullite system, Ceram. Int. 42 (2016) 17067–17073.
[38] K.R. Phillips, N. Vogel, Y. Hu, M. Kolle, C.C. Perry, J. Aizenberg, Tunable anisotropy in inverse opals and emerging optical properties, Chem. Mater. 26 (2014) 1622–1628.
[39] R.K. Bordia, R. Raj, Sintering behavior of ceramic films constrained by a rigid substrate, J. Am. Ceram. Soc. 68 (1985) 287–292.
[40] M.K. Tripp, C. Stampfer, D.C. Miller, T. Helbling, C.F. Herrmann, C. Hierold, K. Gall, S.M. George, V.M. Bright, The mechanical properties of atomic layer deposited alumina for use in micro- and nano-electromechanical systems, Sens. Actuators A 130–131 (2006) 419–429.
[41] G. Krautheim, T. Hecht, S. Jakschik, U. Schröder, W. Zahn, Mechanical stress in ALD-Al_2O_3 films, Appl. Surf. Sci. 252 (2005) 200–204.
[42] V.V. Afanas'ev, A. Stesmans, B.J. Mrstik, C. Zhao, Impact of annealing-induced compaction on electronic properties of atomic-layer-deposited Al_2O_3, Appl. Phys. Lett. 81 (2002) 1678–1680.
[43] Z.-Y. Wang, R.-J. Zhang, H.-L. Lu, X. Chen, Y. Sun, Y. Zhang, Y.-F. Wei, J.-P. Xu, S.-Y. Wang, Y.-X. Zheng, L.-Y. Chen, The impact of thickness and thermal annealing on refractive index for aluminum oxide thin films deposited by atomic layer deposition, Nanoscale Res. Lett. 10 (2015) 46.
[44] G. Rani, P.D. Sahare, Effect of temperature on structural and optical properties of boehmite nanostructure, Int. J. Appl. Ceram. Technol. 12 (2015) 124–132.
[45] J.A. Pask, H. Schneider, Phase equilibria and stability of mullite, in: H. Schneider, S. Komarneni (Eds.), Mullite, John Wiley Distributor, Weinheim, Chichester, 2005, pp. 227–249.
[46] D.R. Clarke, S.R. Phillpot, Thermal barrier coating materials, Mater. Today 8 (2005) 22–29.
[47] K. Wang, M.D. Sacks, Mullite formation by endothermic reaction of alpha-alumina/silica microcomposite particles, J. Am. Ceram. Soc. 79 (1996) 12–16.
[48] E.R. de Sola, F.J. Torres, J. Alarcón, Thermal evolution and structural study of 2, J. Eur. Ceram. Soc. 26 (2006) 2279–2284.
[49] B.D. Cullity, Elements of X-ray Diffraction, 2nd ed., Addison-Wesley Pub. Co., Reading, MA, 1978.
[50] S. Jakschik, U. Schroeder, T. Hecht, M. Gutsche, H. Seidl, J.W. Bartha, Crystallization behavior of thin ALD-Al_2O_3 films, Thin Solid Films 425 (2003) 216–220.
[51] C. Barbos, D. Blanc-Pelissier, A. Fave, E. Blanquet, A. Crisci, E. Fourmond, D. Albertini, A. Sabac, K. Ayadi, P. Girard, M. Lemiti, Characterization of Al_2O_3 thin films prepared by thermal ALD, Energy Procedia 77 (2015) 558–564.
[52] J. Wang, S. Ahl, Q. Li, M. Kreiter, T. Neumann, K. Burkert, W. Knoll, U. Jonas, Structural and optical characterization of 3D binary colloidal crystal and inverse opal films prepared by direct co-deposition, J. Mater. Chem. 18 (2008) 981–988.
[53] A. Lashtabeg, J.L. Bradley, G. Vives, J. Drennan, The effects of templating synthesis procedures on the microstructure of yttria stabilised zirconia (YSZ) and NiO/YSZ templated thin films, Ceram. Int. 36 (2010) 653–659.
[54] W.D. Kingery, B. Francois, The sintering of crystalline oxides. I. Interactions between grain boundaries and pores, in: S. Sōmiya, Y. Moriyoshi (Eds.), Sintering Key Papers, Springer Netherlands, Dordrecht, 1990, pp. 449–466.
[55] E.B. Slamovich, F.E. Lange, Densification of large pores: I, Experiments, J. Am. Ceram. Soc. 75 (2005) 2498–2508.
[56] E.B. Slamovich, F.E. Lange, Densification of large pores: II, Driving potentials and kinetics, J. Am. Ceram. Soc. 76 (2005) 1584–1590.